

Continuum Robot Dynamics Utilizing the Principle of Virtual Power

William S. Rone, *Student Member, IEEE*, and Pinhas Ben-Tzvi, *Senior Member, IEEE*

Abstract—Efficient formulations for the dynamics of continuum robots are necessary to enable accurate modeling of the robot's shape during operation. Previous work in continuum robotics has focused on low-fidelity lumped parameter models, in which actuated segments are modeled as circular arcs, or computationally intensive high-fidelity distributed parameter models, in which continuum robots are modeled as a parameterized spatial curve. In this paper, a novel dynamic modeling methodology is studied that captures curvature variations along a segment using a finite set of kinematic variables. This dynamic model is implemented using the principle of virtual power (also called Kane's method) for a continuum robot. The model is derived to account for inertial, actuation, friction, elastic, and gravitational effects. The model is inherently adaptable for including any type of external force or moment, including dissipative effects and external loading. Three case studies are simulated on a cable-driven continuum robot structure to study the dynamic properties of the numerical model. Cross validation is performed in comparison to both experimental results and finite-element analysis.

Index Terms—Continuum robotics, cable-driven actuation, computational dynamics, principle of virtual power.

I. INTRODUCTION

CONTINUUM robots pose significant challenges in modeling their dynamics in comparison to conventional robots with discrete joints, even those with link and/or joint flexibility modeled [1], [2]. The importance of elastic effects in continuum robots, at the same level of actuation and gravity, complicates the analysis. Furthermore, the robot's continuum nature leads to theoretically infinite degrees of freedom. Despite these challenges, continuum robots demonstrate numerous advantages over discrete-joint structures, including greater shape flexibility, higher compliance, and whole-arm manipulation capabilities. S. Hirose, a pioneer in studying these snake-like structures, wrote that these structures possess "hitherto nonexistent functions—impossible with a conventional industrial robot" including "twining around an object" [3]. In order to better use these robots, methods are needed to formulate the robot's dynamics in a tractable form.

Manuscript received March 28, 2013; revised July 15, 2013; accepted September 7, 2013. Date of publication September 27, 2013; date of current version February 3, 2014. This paper was recommended for publication by Associate Editor N. Simaan and Editor B. J. Nelson upon evaluation of the reviewers' comments. This work was supported in part by the National Science Foundation under Grant No. 1334227.

The authors are with the George Washington University, Washington, DC 20037 USA (e-mail: wsrone@gwu.edu; bentzvi@gwu.edu).

Color versions of one or more of the figures in this paper are available online at <http://ieeexplore.ieee.org>.

Digital Object Identifier 10.1109/TRO.2013.2281564

Previous efforts to model continuum robot motion may be categorized into two approaches: low-fidelity lumped parameter models and high-fidelity distributed parameter models. The low-fidelity lumped parameter models assume that each actuated segment of the robot may be characterized by a single circular arc. The high-fidelity distributed model represents the continuum robot with a spatial parameterized curve or a 3-D volume. Purely kinematic models have been derived for the lumped parameter models, static models have been derived for the distributed parameter models, and dynamic models have been derived for both.

The previously studied lumped parameter models are characterized as low fidelity because they ignore the curvature variations along the length of the robot due to loading such as gravity, friction, or contact forces. Webster and Jones [4] provide a review of constant-curvature kinematic methods for continuum robots that feature direct analytical calculation of continuum segment shape using actuation inputs for different actuation structures (e.g., cable or rod displacement, pneumatic bellow pressure). Chirikjian and Burdick [5] explore an alternative kinematic approach, where Bessel functions are used to generate configurations, and a serpentine robot is shaped to those curves. Previous work has also studied lumped parameter dynamic models. Tatlicioglu *et al.* [6] and Godage *et al.* [7] adapted the Euler–Lagrange equations by formulating a Lagrangian from the kinetic energy (due to continuum robot motion), potential energy (due to elasticity and gravity), and actuation effects for pneumatic [6] and hydraulic [7] continuum robots.

The previously studied distributed parameter models are characterized as high fidelity because they allow for an arbitrary shape of the continuum robot in response to the applied loading. Time-invariant static formulations have been studied extensively using a variety of analytical methods. Jones *et al.* [8] and Renda *et al.* [9] utilized Cosserat rod theory to represent the robot as a 1-D curve in space, with relevant elastic, actuation, and gravitational forces considered for a cable-driven robot. Rucker *et al.* [10] determined equilibrium configuration by tracking the local minimization of an energy function during the robot's motion for a concentric tube robot. In addition, dynamic models have been studied to also account for inertial effects. Building on previous statics models, Rucker and Webster [11], Spillmann and Spillmann [12] and Lang *et al.* [13] formulated dynamic Cosserat rod models, resulting in coupled partial differential equations (PDEs). Unlike previous approaches for cable-driven robots [8], Rucker and Webster [11] augment the conventional point-moment actuation loading at the tip with a distributed force due to the cable routing along the robot. Chirikjian [14] approximates a serpentine manipulator as a continuum body

and formulates the dynamics utilizing continuum mechanics conservation equations. Gravagne *et al.* [15] utilized Hamilton's principle to formulate the dynamics as a set of PDEs for a cable-driven robot.

Structures previously considered have included cable-driven, rod-driven, pneumatic/hydraulic-driven, and concentric-tube robots. Cable-driven robots have a backbone (such as a pneumatic tube [16] or elastic rod [17]) with cabling along the robot's length and attached at the end of its segment. Rod-driven robots [18], [19] use elastic rods to transmit actuation from the base along the robot, increasing the robot's stiffness. Pneumatic and hydraulic continuum robots [7], [20]–[23] utilize segments that are composed of pneumatic/hydraulic “muscles” to bend into varying shapes. Concentric-tube robots [24], [25] are composed of precurved elastic tubes arranged concentrically. By controlling the relative orientation and displacement of the tubes their shape is controlled.

A. Contribution

In this paper, a novel high-fidelity, lumped parameter model for discretizing a continuum robot to formulate the continuum robot dynamics using the principle of virtual power is presented. Instead of modeling a continuum robot segment as a single circular arc, a serial chain of subsegment circular arcs defines the segment shape. This provides a systematic way to discretize the continuum robot into a set of generalized coordinates and is capable of incorporating actuation, friction, elastic, and gravitational mechanical effects. Xu and Simaan [26] previously used subsegment-based analysis for the statics of a rod-driven continuum robot. However, the governing equations were required to be solved using an optimization solver, limiting the method's utility for real-time calculation. In this paper, a cable-driven continuum robot is analyzed using this methodology; although the approach is applicable to any continuum robotic structure. The resulting model is a set of coupled first-order ordinary differential equations (ODEs) in time that may be numerically integrated to calculate the dynamic response. This paper builds on the authors' previous work in [27], in which a model for the static equilibrium of a planar continuum robot was derived using the principle of virtual work. This study presents a spatial model of the dynamics that is derived using the principle of virtual power.

The primary benefit of the proposed high-fidelity lumped parameter subsegment model is the balance it achieves between the previous low-fidelity lumped parameter and high-fidelity distributed parameter models. Like the lumped parameter models, the continuum robot shape is defined by a finite set of variables, instead of a parameterized spatial curve like the distributed parameter model. However, the proposed model can also capture variation in curvature along the robot's length, unlike previous lumped parameter models. In addition, unlike the distributed parameter models, the dynamic equations of motion using the subsegment modeling approach results in a set of coupled ODEs in time, instead of PDEs in time and space.

In addition, there are also benefits to the modeling approach that stem from the use of the method of virtual power. Unlike the Newton–Euler method, explicit internal force calculations

are not needed at each disk, improving computational efficiency. Unlike the Euler–Lagrange method, the method of virtual power can directly incorporate nonconservative effects into the equations of motion, instead of requiring differentiable energy loss functions that complicate the analysis.

B. Outline

Section II outlines the principle of virtual power and describes the cable-driven continuum robot considered in this study. Section III derives the continuum robot's kinematics. Section IV derives the mechanical effects governing the continuum robot's behavior, including inertia, elasticity, gravity, actuation loading, and friction. Section V describes the numerical implementation of the model. Section VI details the cross-validation of the virtual power method simulations compared with numerical models and experimental results. Section VII summarizes this study and describes the future work.

II. BACKGROUND

A. Principle of Virtual Power (Kane's Method)

The method of virtual power, also called Kane's method, uses variational calculus to calculate the dynamics of a system by minimizing the virtual power of the external forces and moments applied to the system [28], and it has been previously applied to both rigid-link [29], [30] and flexible [31] robotic systems. This scalar virtual power P is found by adding the dot products of each rigid body i 's net external moment $\mathbf{M}_{i,ex}$ and force $\mathbf{F}_{i,ex}$ with the associated angular $\boldsymbol{\omega}_i$ and linear \mathbf{v}_i velocities at the body's center of mass, as shown in (1). To take the variation, the generalized coordinates q_k and velocities u_k are chosen to define the dynamic configuration of the system. In cases where the generalized velocities are not the derivatives of the generalized coordinates, a unique mapping $u_k = A_{kl}\dot{q}_l$ is needed. In this paper, $u_k = \dot{q}_k$

$$P = \sum_i (\mathbf{M}_{i,ex} \cdot \boldsymbol{\omega}_i + \mathbf{F}_{i,ex} \cdot \mathbf{v}_i). \quad (1)$$

The angular and linear velocities of each rigid body may be defined with respect to the generalized velocities using the partial angular velocity $\boldsymbol{\omega}_{i,k}$ and the partial linear velocity $\mathbf{v}_{i,k}$, as in (2), shown below. Using this velocity formulation, the virtual power variation ΔP may be found as in (3), shown below. To minimize the virtual power, $\Delta P = 0$. For this to be true for any arbitrary generalized velocity variation $\Delta\dot{q}_k$, (4), shown below, must be true, providing the governing equations for the dynamics, with one equation defined for each coordinate k

$$\boldsymbol{\omega}_i = \sum_k \boldsymbol{\omega}_{i,k} \dot{q}_k, \quad \mathbf{v}_i = \sum_k \mathbf{v}_{i,k} \dot{q}_k \quad (2)$$

$$\Delta P = \sum_k \left(\left[\sum_i (\mathbf{M}_{i,ex} \cdot \boldsymbol{\omega}_{i,k} + \mathbf{F}_{i,ex} \cdot \mathbf{v}_{i,k}) \right] \Delta\dot{q}_k \right) \quad (3)$$

$$\sum_i (\mathbf{M}_{i,ex} \cdot \boldsymbol{\omega}_{i,k} + \mathbf{F}_{i,ex} \cdot \mathbf{v}_{i,k}) = 0. \quad (4)$$

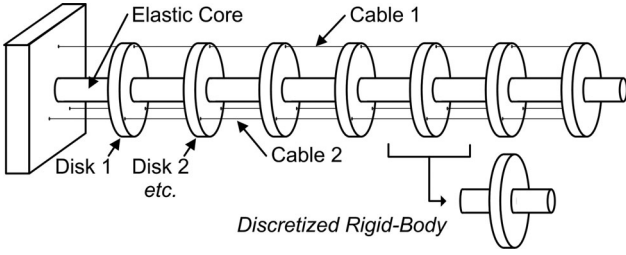


Fig. 1. Cable-driven continuum robotic structure under consideration with rigid-body discretization illustrated.

The external moments and forces are composed of two types of effects: inertial and active. Inertial effects are due to the rigid bodies' resistance to changes in acceleration. Active effects are due to either physical effects (such as elasticity or friction) or external loading (such as actuation, gravity, or contact forces). If a force is applied to the body at a point other than its center of gravity, an equivalent force and moment at the center of gravity may be calculated. To find the net external moment $\mathbf{M}_{i,ex}$ and force $\mathbf{F}_{i,ex}$ on each body, the inertial and active forces and moments are added together. A key benefit of the method of virtual power is its ability to directly include moments and forces in the mechanics calculation: as long as a moment or force vector can be calculated, it can be added to the net external moment or force terms. In addition, this model may also be used to formulate a time-invariant model of the continuum robot static equilibrium by neglecting the inertial effects.

B. Cable-Driven Continuum Robotic Structure

The cable-driven continuum robot under consideration is illustrated in Fig. 1. An elastic core is the robot's backbone, along which are rigidly mounted disks. Three cables actuate the robot. This structure leads to a natural choice for the discretization into subsegments with each disk modeled as a rigid body. The mass and inertia of each rigid body are determined by the mass and inertia of the disk, and elastic core surrounding the disk, which is illustrated in Fig. 1. The kinematics assumes circular subsegment arcs separate each rigid body. Based on the elastic core properties, each subsegment's modeled elastic effects (bending and torsion) apply moments to the subsegment's two adjacent disks. Compressive and shear loads are neglected due to the incompressibility of the modeled elastic core compared with its bending and twist. Gravitational loading will be applied at each disk's center of mass. Actuation and cable-disk friction will be calculated as a force and moment at each disk's center of mass.

III. KINEMATIC ANALYSIS

In this section, the kinematics of the continuum robot, including positions, velocities, and accelerations, are derived.

A. Local Coordinates, Linear Position, and Angular Velocity

As discussed in Section II-A, a set of generalized coordinates and velocities are needed to describe the dynamic configuration of the system. Based on the subsegment discretization in Section

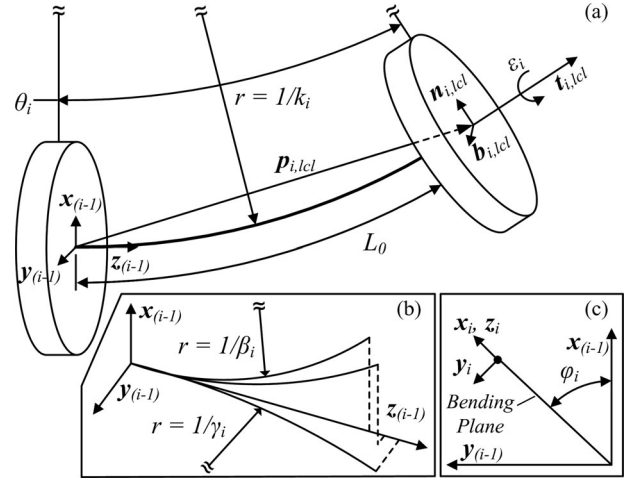


Fig. 2. (a) Segment coordinates and frames on two sequential disks. The coordinate frames are illustrated on the disks' surfaces for clarity—their origins actually align with the disks' centers of mass. (b) Composition of the resulting segment curvature by its two orthogonal curvatures β_i and γ_i . (c) Illustration showing the bending plane angle φ_i .

II-B, three scalar coordinates are used to describe the difference in position and orientation between two adjacent disks: two orthogonal subsegment curvatures β_i and γ_i and the subsegment twist angle ε_i . A vector $\mathbf{q}_{i,lcl}$ of these three variables defines the generalized coordinates for a given subsegment, as in (5), shown below, and the collection of these vectors for an N -subsegment continuum robot results in the robot's generalized coordinates \mathbf{q} , shown below in (6):

$$\mathbf{q}_{i,lcl} = [\beta_i, \gamma_i, \varepsilon_i]^T \quad (5)$$

$$\mathbf{q} = [\mathbf{q}_{1,lcl}^T, \mathbf{q}_{2,lcl}^T, \dots, \mathbf{q}_{N,lcl}^T]^T \quad (6)$$

To simplify the analysis, three intermediate variables are defined in (7), shown below: 1) the subsegment curvature magnitude k_i ; 2) the bending plane angle φ_i ; and 3) the subsegment bending angle θ_i , where L_0 is the subsegment length. The atan2 function is a four quadrant mapping of the two quadrant $\text{atan}(\gamma_i/\beta_i)$ function

$$k_i = \sqrt{\beta_i^2 + \gamma_i^2}, \quad \varphi_i = \text{atan2}(\gamma_i, \beta_i) \quad \theta_i = k_i L_0. \quad (7)$$

An illustration of these parameters is shown in Fig. 2. Each disk has a local coordinate system coincident with its center of mass (Fig. 2 illustrates these frames on the surfaces for clarity). For disk i , the local coordinate system is $x_i y_i z_i$. The global frame at the robot's base is denoted by $x_0 y_0 z_0$.

Based on geometric analysis [4], the local position vector $\mathbf{p}_{i,lcl}$ of the disk i center of mass relative to the previous frame $i-1$ is calculated in (8), shown below. For this and other expressions, special consideration must be made for cases in which $k_i = 0$. Analytically, the expressions all become zero divided by zero. However, as $\lim_{k \rightarrow 0}$, the coordinates asymptotically approach $\mathbf{p}_{i,lcl} = [0, 0, L_0]^T$. In numerical solvers, this singularity (and others throughout the analysis) may be avoided by a substitution of the asymptotic values when k_i is near zero. In addition, based on this lumped parameter modeling approach, the torsion does not contribute to the subsegment's position

vector. Instead, it is incorporated as a rotation between subsegments as described next.

$$\mathbf{p}_{i,lcl} = [c_{\varphi_i} (1 - c_{\theta_i})/k_i, \quad s_{\varphi_i} (1 - c_{\theta_i})/k_i, \quad s_{\theta_i}/k_i]^T. \quad (8)$$

In order to define the orientation, the local unit vectors of frame i in the frame $i-1$ are used. Three sequential rotations are used to compose the local rotation matrix $\mathbf{R}_{i,lcl}$: a rotation by φ_i around the original z_{i-1} , followed by a rotation by θ_i around the current y -axis, followed by a rotation by $(\varepsilon_i - \varphi_i)$ around the current z_i -axis, as in

$$\mathbf{R}_{i,lcl} = \begin{bmatrix} c_{\varphi_i} & -s_{\varphi_i} & 0 \\ s_{\varphi_i} & c_{\varphi_i} & 0 \\ 0 & 0 & 1 \end{bmatrix} \begin{bmatrix} c_{\theta_i} & 0 & -s_{\theta_i} \\ 0 & 1 & 0 \\ s_{\theta_i} & 0 & c_{\theta_i} \end{bmatrix} \times \begin{bmatrix} c_{\varepsilon_i - \varphi_i} & -s_{\varepsilon_i - \varphi_i} & 0 \\ s_{\varepsilon_i - \varphi_i} & c_{\varepsilon_i - \varphi_i} & 0 \\ 0 & 0 & 1 \end{bmatrix}. \quad (9)$$

The local angular velocity $\boldsymbol{\omega}_{i,lcl}$ is defined based on the motion of the tangent vector $\mathbf{t}_{i,lcl}$ and the twist angular velocity $\dot{\varepsilon}_i$ about $\mathbf{t}_{i,lcl}$. The cross product of $\boldsymbol{\omega}_{i,lcl}$ and $\mathbf{t}_{i,lcl}$ is $\dot{\mathbf{t}}_{i,lcl}$, whereas the dot product is $\dot{\varepsilon}_i$, as in (10) and (11), shown below. An explicit expression for $\boldsymbol{\omega}_{i,lcl}$ may be found by simplifying the cross product of $\mathbf{t}_{i,lcl}$ and $\boldsymbol{\omega}_{i,lcl} \times \mathbf{t}_{i,lcl}$, as in (12), shown below.

$$\dot{\mathbf{t}}_{i,lcl} = \boldsymbol{\omega}_{i,lcl} \times \mathbf{t}_{i,lcl} \quad (10)$$

$$\dot{\varepsilon}_i = \boldsymbol{\omega}_{i,lcl} \cdot \mathbf{t}_{i,lcl} \quad (11)$$

$$\begin{aligned} \mathbf{t}_{i,lcl} \times (\boldsymbol{\omega}_{i,lcl} \times \mathbf{t}_{i,lcl}) &= (\mathbf{t}_{i,lcl} \cdot \mathbf{t}_{i,lcl}) \boldsymbol{\omega}_{i,lcl} \\ &\quad - (\mathbf{t}_{i,lcl} \cdot \boldsymbol{\omega}_{i,lcl}) \mathbf{t}_{i,lcl} \\ \boldsymbol{\omega}_{i,lcl} &= \mathbf{t}_{i,lcl} \times \dot{\mathbf{t}}_{i,lcl} + \dot{\varepsilon}_i \mathbf{t}_{i,lcl}. \end{aligned} \quad (12)$$

B. Global Positions, Velocities, and Accelerations

Rotation matrices \mathbf{R}_i for each disk's orientation may be found recursively, as shown in (13) below. Using these global rotations, each disk i position \mathbf{p}_i and angular velocity $\boldsymbol{\omega}_i$ are found recursively in (14) and (15), shown below.

$$\mathbf{R}_i = \begin{cases} \mathbf{R}_{i,lcl}, & i = 1 \\ \mathbf{R}_{i-1} \mathbf{R}_{i,lcl}, & i > 1 \end{cases} \quad (13)$$

$$\mathbf{p}_i = \begin{cases} \mathbf{p}_{i,lcl}, & i = 1 \\ \mathbf{p}_{i-1} + \mathbf{R}_{i-1} \mathbf{p}_{i,lcl}, & i > 1 \end{cases} \quad (14)$$

$$\boldsymbol{\omega}_i = \begin{cases} \boldsymbol{\omega}_{i,lcl}, & i = 1 \\ \boldsymbol{\omega}_{i-1} + \mathbf{R}_{i-1} \boldsymbol{\omega}_{i,lcl}, & i > 1. \end{cases} \quad (15)$$

To simplify the following analyses, it should be noted that $\dot{\mathbf{R}}_i$ may be replaced by the cross product in (16), shown below. Each disk's linear velocity \mathbf{v}_i and angular acceleration $\boldsymbol{\alpha}_i$ are found by taking the derivative of (14) and (15), as in (17) and (18), shown below, and the disks' linear acceleration $\boldsymbol{\alpha}_i$ are found by taking the derivative of (17), as in (19) shown below.

$$\dot{\mathbf{R}}_i = \boldsymbol{\omega}_i \times \mathbf{R}_i \quad (16)$$

$$\mathbf{v}_i = \begin{cases} \dot{\mathbf{p}}_{i,lcl}, & i = 1 \\ \mathbf{v}_{i-1} + \boldsymbol{\omega}_{i-1} \times \mathbf{R}_{i-1} \mathbf{p}_{i,lcl} + \mathbf{R}_{i-1} \dot{\mathbf{p}}_{i,lcl}, & i > 1 \end{cases} \quad (17)$$

$$\boldsymbol{\alpha}_i = \begin{cases} \dot{\boldsymbol{\omega}}_{i,lcl} & i = 1 \\ \boldsymbol{\alpha}_{i-1} + \boldsymbol{\omega}_{i-1} \times \mathbf{R}_{i-1} \boldsymbol{\omega}_{i,lcl} + \mathbf{R}_{i-1} \dot{\boldsymbol{\omega}}_{i,lcl}, & i > 1 \end{cases} \quad (18)$$

$$\mathbf{a}_i = \begin{cases} \ddot{\mathbf{p}}_{i,lcl}, & i = 1 \\ \left(\begin{array}{l} \mathbf{a}_{i-1} + \dot{\boldsymbol{\omega}}_{i-1} \times \mathbf{R}_{i-1} \mathbf{p}_{i,lcl} + 2\boldsymbol{\omega}_{i-1} \\ \quad \times \mathbf{R}_{i-1} \dot{\mathbf{p}}_{i,lcl} + \boldsymbol{\omega}_{i-1} \\ \quad \times (\boldsymbol{\omega}_{i-1} \times \mathbf{R}_{i-1} \mathbf{p}_{i,lcl}) + \mathbf{R}_{i-1} \ddot{\mathbf{p}}_{i,lcl} \end{array} \right), & i > 1. \end{cases} \quad (19)$$

In addition, to simplify the analysis in Section IV, the three unit vectors that are associated with each coordinate frame are denoted $\hat{\mathbf{x}}_i$, $\hat{\mathbf{y}}_i$, and $\hat{\mathbf{z}}_i$, as in (20), shown below. For $i = 0$, \mathbf{R}_0 equals the identity matrix

$$[\hat{\mathbf{x}}_i, \hat{\mathbf{y}}_i, \hat{\mathbf{z}}_i] = \mathbf{R}_i. \quad (20)$$

IV. EXTERNAL LOADING ANALYSIS

In this section, the external loading forces $\mathbf{F}_{i,ex}$ and moments $\mathbf{M}_{i,ex}$ on the continuum robot are formulated, including inertia, elasticity, gravity, actuation, and friction.

A. Inertial Effects

Inertial effects account continuum robot's resistance to changing the linear and angular velocities. Equations (21) and (22), shown below, define each disk's inertial force $\mathbf{F}_{i,inr}$ and moment $\mathbf{M}_{i,inr}$, where m_i is the disk's mass and \mathbf{I}_i is the disk's moment of inertia. \mathbf{I}_i depends on the disk orientation and the local radial $I_{xx,lcl}$ and axial $I_{zz,lcl}$ moments of inertia, as in (23), shown below.

$$\mathbf{F}_{i,inr} = -m_i \mathbf{a}_i \quad (21)$$

$$\mathbf{M}_{i,inr} = -\mathbf{I}_i \boldsymbol{\alpha}_i - \boldsymbol{\omega}_i \times \mathbf{I}_i \boldsymbol{\omega}_i \quad (22)$$

$$\mathbf{I}_i = \mathbf{R}_i \begin{bmatrix} I_{xx,lcl} & 0 & 0 \\ 0 & I_{xx,lcl} & 0 \\ 0 & 0 & I_{zz,lcl} \end{bmatrix} \mathbf{R}_i^T. \quad (23)$$

B. Elastic Effects

Elastic effects account for the forces and moments that are generated internally within the continuum core in response to deformation. The choice of the generalized coordinates allow for the direct calculation of bending and torsion.

The bending moment magnitude of subsegment i is proportional to k_i , with the proportionality constant EJ_{xx} , where E is Young's modulus and J_{xx} is the core cross section's second moment of area. The bending moment direction is normal to the bending plane defined by φ_i , leading to the bending moment $\mathbf{M}_{i,bnd}$, defined as

$$\mathbf{M}_{i,bnd} = EJ_{xx} k_i \mathbf{R}_{i-1} [-s_{\varphi_i}, \quad c_{\varphi_i} \quad 0]^T. \quad (24)$$

The torsional moment magnitude of subsegment i is proportional to the subsegment twist angle ε_i , with the constant of

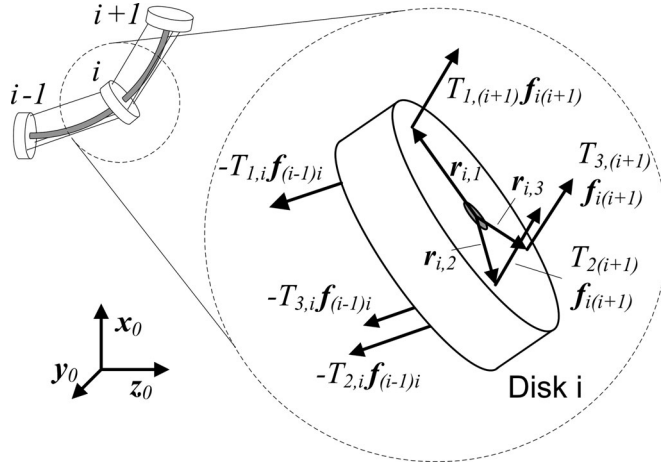


Fig. 3. Actuation cabling between disks. Each cable exerts a force at the routing hole based on the relative location of the adjacent disks' routing holes.

proportionality GJ_{zz}/L_0 , where G is the shear modulus and J_{zz} is the core cross section's polar moment of area. For a given subsegment i , the moments at each end $M_{i:(i-1),tor}$ and $M_{i:i,tor}$, will affect disks $i-1$ and i , as defined in

$$M_{i:(i-1),tor} = GJ_{zz} \varepsilon_i \hat{z}_{i-1}/L_0, \quad M_{i:i,tor} = -GJ_{zz} \varepsilon_i \hat{z}_i/L_0. \quad (25)$$

The elastic loading at each disk is due to the sum of these two effects due to the adjacent subsegment(s). An equation for the resulting elastic moment $M_{i,el}$ is shown as

$$M_{i,el} = \begin{cases} M_{i:i,tor} + M_{(i+1):i,tor} \\ \quad + M_{i+1,bnd} - M_{i,bnd}, & i < N \\ M_{i:i,tor} - M_{i,bnd}, & i = N. \end{cases} \quad (26)$$

C. Gravitational Loading

Gravitational loading accounts for the body forces on the robot due to gravity. The force on each disk $F_{i,gr}$, shown in (27), shown below, is applied at each disk's center of mass relative to the global frame, where g is the gravitational constant

$$F_{i,gr} = -m_i g \hat{x}_0. \quad (27)$$

D. Actuation Loading: Contact Forces and Friction

Actuation loading accounts for the force and moment on each disk due to the tensions of the three actuation cables. In addition, the contact forces between the disk and cabling also results in frictional forces. The resulting force at the disks' cable routing holes are reformulated as a resultant force and moment acting at the disk center of mass.

When considering cable-actuated robots, it is important to ensure that the model does not allow for compressive forces by the actuation cabling. In this model, the tensions of the actuation cables at the base are the input parameters to the model. By ensuring that these inputs are always positive tension inputs, the cabling cannot apply a compressive force.

A geometric analysis is used to determine the loading on each disk. Fig. 3 shows the cable routing between three disks. Because the cables follow a linear path between holes, the cable routing

may be determined by calculating the hole coordinates. At the continuum robot base and within each local disk frame, the three cable routing hole position vectors— $r_{lcl,1}$, $r_{lcl,2}$, and $r_{lcl,3}$ —are defined by (28), shown below, where r_h is the radial distance of the holes from the center

$$\begin{aligned} r_{lcl,1} &= r_h [1, 0, 0], & r_{lcl,2} &= r_h [-1/2, \sqrt{3}/2, 0] \\ r_{lcl,3} &= r_h [-1/2, -\sqrt{3}/2, 0]. \end{aligned} \quad (28)$$

Using the $p_{i,lcl}$, the position $p_{i,j,hl}$ of the j th cable in the i th subsegment may be calculated using (29), shown below. As a result, the cable force directions $f_{i,j}$ may be found as the unit vector of $p_{i,j,hl}$, defined in (30), shown below, and shown in Fig. 3.

$$p_{i,j,hl} = \begin{cases} p_{i,lcl} + R_i r_{lcl,j} - r_{lcl,j}, & i = 1 \\ R_{i-1} p_{i,lcl} + R_i r_{lcl,j} - R_{i-1} r_{lcl,j}, & i > 1 \end{cases} \quad (29)$$

$$f_{i,j} = p_{i,j,hl} / \|p_{i,j,hl}\|. \quad (30)$$

The coupling of the cable tension along the continuum robot and the frictional forces at each disk complicates the analysis. In order to compute the friction at each disk, the average tension of the cable before and after the disk is needed. However, in order to compute the cable tensions before and after the disk, the magnitude of the frictional force is needed. Therefore, an iterative approach is required. The initial assumption will be that tension is constant along the continuum robot. Based on this assumption, the contact friction will be estimated for each cable at each disk. This contact friction estimate will then be used to update the cable tensions in each subsegment along the length of the continuum robot. These updated tensions will then be used to update the friction estimate. Section V will include the analysis on the ‘‘convergence’’ of the resulting subsegment cable tensions based on the number of iterations of this process and will determine the optimal number to balance the need for an accurate computation with the need to reduce the computational load of the model.

In this analysis, the conventional discontinuous stick-slip friction model will be replaced by a continuous saturated viscous friction model. This enables the model to accurately represent the dynamic sliding friction when the cable sliding velocity is not near zero, while ensuring a continuous force profile when the sliding direction changes. This approach does not allow for a greater static friction than dynamic sliding frictional force, as is normally observed in mechanical systems, but significantly simplifies the dynamic analysis in this initial study.

Due to the ‘‘wrap’’ of the cabling around the cable routing holes, as illustrated in Fig. 4(a), a belt friction model is used in this analysis. Fig. 4(b) shows an illustration of the key model parameters, and (31), shown below, provides the numerical expression of the model, where μ is the coefficient of saturated viscous friction and $\eta_{i,j}$ is the contact angle defined in (32), shown below. Based on (31), (33), shown below, may be formulated to determine the magnitude of the frictional force $F_{i,j,fr}$ at the j th hole of the i th disk. This magnitude is the difference in the left and right tensions $T_{i,j}$ and $T_{(i+1),j}$. A key benefit of this approach is that it allows the solver to estimate the frictional

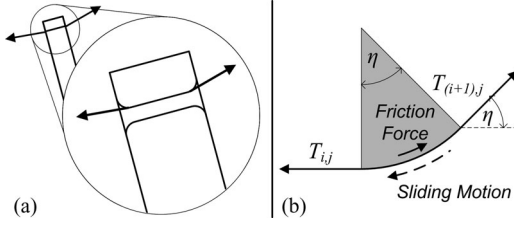


Fig. 4. (a) Cut-away view of cable-disk contact. (b) Assumed belt friction model for cable-disk contact.

force magnitude with estimates for the left and right tensions. For example, in the initial case, the left and right tensions are assumed to be equal. The difference of these tensions is identically zero; however, (33) will estimate the frictional force based on the sum of these two tensions

$$T_{i,j}/T_{i+1,j} = e^{\mu\eta_{i,j}} \quad (31)$$

$$\eta_{i,j} = \cos^{-1}(\mathbf{f}_{i,j} \cdot \mathbf{f}_{i+1,j}) \quad (32)$$

$$\|\mathbf{F}_{i,j,fr}\| = (T_{i,j} + T_{i+1,j})(e^{\mu\eta_{i,j}} - 1)/(e^{\mu\eta_{i,j}} + 1). \quad (33)$$

In order to determine the direction of the sliding motion at each disk, the rate of change of each subsegment's cable lengths will be calculated. For cable j in subsegment i , $d_{i,j,ss}$ is the subsegment cable length, as in (34), shown below. The derivative of this length in (35), shown below, can be used to recursively calculate the cable sliding velocity from the terminal disk to the base. Because the cable is tied to the final disk, there will be zero sliding velocity at this disk. For the next disk, the sliding velocity is the sum of the following disk's cable sliding velocity plus the cable length derivative of the subsegment separating these disks, as in (36), shown below.

$$d_{i,j,ss}^2 = \mathbf{p}_{i,j,hl} \cdot \mathbf{p}_{i,j,hl} \quad (34)$$

$$\dot{d}_{i,j,ss} = (\mathbf{p}_{i,j,hl} \cdot \dot{\mathbf{p}}_{i,j,hl}) / \dot{d}_{i,j,ss} \quad (35)$$

$$\dot{d}_{i,j,dsk} = \begin{cases} 0, & i = N \\ \dot{d}_{i+1,j,dsk} + \dot{d}_{i+1,j,ss}, & i < N. \end{cases} \quad (36)$$

With this estimate of the friction magnitude and the cable-disk sliding velocities, a recursive calculation can be used to determine the cable tensions in each cable and subsegment. Beginning from the applied tension $T_{j,app}$ at the continuum robot base for each cable j , (37), shown below, shows how the calculated friction magnitude is subtracted from this tension at each disk until the terminal disk. Because the cabling is rigidly attached to the terminal disk, there is no contact friction present at that disk. A saturation function $sat(\dot{d}_{i,j,dsk})$, defined in (38), shown below, is used to determine the scaling and direction of the friction force. This replaces the discontinuous signum function, which returns the unit positive or negative based on the velocity's sign. This creates a continuous function over zero for the switching between directions

$$T_{i,j} = \begin{cases} T_{j,app}, & i = 1 \\ T_{i-1,j} - sat(\dot{d}_{i,j,dsk}) \|\mathbf{F}_{i,j,fr}\|, & i > 1 \end{cases} \quad (37)$$

$$sat(\dot{d}_{i,j,dsk}) = \begin{cases} \dot{d}_{i,j,dsk}/\dot{d}_{sat}, & \|\dot{d}_{i,j,dsk}/\dot{d}_{sat}\| \leq 1 \\ \text{sgn}(\dot{d}_{i,j,dsk}), & \|\dot{d}_{i,j,dsk}/\dot{d}_{sat}\| > 1. \end{cases} \quad (38)$$

With these updated values of $T_{i,j}$, (33) can be used to calculate more accurate estimates of the frictional force magnitude at each disk, which then may be used to calculate more accurate cable tensions using (37).

Once a sufficient number of iterations has occurred (the determination of a sufficient number is addressed in Section V), the contact force $\mathbf{F}_{i,j,con}$ which includes frictional effects may be determined for each cable and disk, as in (39), shown below, with the two forces shown in Fig. 3

$$\mathbf{F}_{i,j,con} = \begin{cases} T_{i+1,j} \mathbf{f}_{i(i+1),j} - T_{i,j} \mathbf{f}_{(i-1)i,j}, & i < N \\ -T_{i,j} \mathbf{f}_{(i-1)i,j}, & i = N. \end{cases} \quad (39)$$

Using the calculated contact and friction forces applied at each disk's cable routing hole, the resulting actuation force $\mathbf{F}_{i,act}$ and moment $\mathbf{M}_{i,act}$ on the disk's center of mass may be computed, as follows:

$$\mathbf{F}_{i,act} = \sum_j \mathbf{F}_{i,j,con}, \quad \mathbf{M}_{i,act} = \sum_j \mathbf{r}_{i,j} \times \mathbf{F}_{i,j,con}. \quad (40)$$

E. Total External Loading

In order to formulate the net external force $\mathbf{F}_{i,ex}$ and moment $\mathbf{M}_{i,ex}$ applied to each disk i , the calculated forces and moments are added together, as in

$$\begin{aligned} \mathbf{F}_{i,ex} &= \mathbf{F}_{i,inr} + \mathbf{F}_{i,gr} + \mathbf{F}_{i,act}, \\ \mathbf{M}_{i,ex} &= \mathbf{M}_{i,inr} + \mathbf{M}_{i,el} + \mathbf{M}_{i,act}. \end{aligned} \quad (41)$$

V. NUMERICAL SIMULATIONS

In this section, the virtual power continuum robot dynamics model is implemented in MATLAB and three case studies are presented: zero, in-plane, and out-of-plane actuation.

A. Numerical Implementation

This modeling approach results in a set of coupled second-order ODEs in time due to the angular and linear acceleration terms in the inertial effects model. In order to solve this series of equations in MATLAB using the built-in ODE solver [32], the equations must be reorganized into the form shown in (42), shown below, where \mathbf{M}_{wgt} is the weighting matrix, and \mathbf{V}_{wgt} is the forcing function vector

$$\mathbf{M}_{wgt}(\mathbf{q}, \dot{\mathbf{q}}) \ddot{\mathbf{q}} = \mathbf{V}_{wgt}(\mathbf{q}, \dot{\mathbf{q}}). \quad (42)$$

The disk's angular and linear accelerations shown in (18) and (19) may be reorganized into the forms shown in (43), shown below, which are the derivatives of (2). Because the terms $\boldsymbol{\omega}_{i,k}$ and $\mathbf{v}_{i,k}$ depend solely on q_k , their derivatives will only be functions of q_k and \dot{q}_k . Therefore, only the terms linear in \ddot{q}_k will depend on \ddot{q}_k

$$\boldsymbol{\alpha}_i = \sum_k (\dot{\boldsymbol{\omega}}_{i,k} \dot{q}_k + \boldsymbol{\omega}_{i,k} \ddot{q}_k), \quad \mathbf{a}_i = \sum_k (\dot{\mathbf{v}}_{i,k} \dot{q}_k + \mathbf{v}_{i,k} \ddot{q}_k). \quad (43)$$

TABLE I
 MATERIAL AND GEOMETRIC PROPERTIES OF EXPERIMENTAL PROTOTYPE

	Property	Value		Property	Value		Property	Value
m_i	Disk and Subsegment Mass	$1.669 \cdot 10^{-3}$ kg	$J_{xx,cl}$	Disk and Subsegment Radial Moment of Inertia	$9.821 \cdot 10^{-8}$ kg·m ²	$I_{zz,cl}$	Disk and Subsegment Axial Moment of Inertia	$1.654 \cdot 10^{-7}$ kg·m ²
J_{xx}	Core Second Moment of Area	$5.743 \cdot 10^{-14}$ m ⁴	J_{zz}	Core Polar Moment of Area	$1.149 \cdot 10^{-13}$ m ⁴	L_0	Initial Subsegment Length (Disk Spacing)	30 mm
E	Core Young's Modulus	$2.1 \cdot 10^{11}$ Pa	G	Core Shear Modulus	$8 \cdot 10^{10}$ Pa	g	Gravitational Acceleration	9.81 m/s ²
r_h	Routing Hole Radius	12.5 mm	μ	Coefficient of Friction	0.15	\dot{d}_{sat}	Saturation velocity limit	0.05 m/s

As a result, the inertial forces and moments will be composed of two terms: a matrix to help formulate \mathbf{M}_{wgt} and a vector contributing to \mathbf{V}_{wgt} . The matrix components $\mathbf{F}_{i,inr:m}$ and $\mathbf{M}_{i,inr:m}$ of $\mathbf{F}_{i,inr}$ and $\mathbf{M}_{i,inr}$ are as in (44), shown below, and the vector components $\mathbf{F}_{i,inr:v}$ and $\mathbf{M}_{i,inr:v}$ are as in (45), shown below. The resulting $\mathbf{F}_{i,inr}$ and $\mathbf{M}_{i,inr}$ are as in (46), shown below.

$$\mathbf{M}_{i,inr:m} = -\mathbf{I}_i \boldsymbol{\omega}_{i,k}, \quad \mathbf{F}_{i,inr:m} = -m_i \mathbf{v}_{i,k} \quad (44)$$

$$\mathbf{M}_{i,inr:v} = -\mathbf{I}_i \dot{\boldsymbol{\omega}}_{i,k} \dot{\mathbf{q}}_k - \boldsymbol{\omega}_i \times \mathbf{I}_i \boldsymbol{\omega}_i$$

$$\mathbf{F}_{i,inr:v} = -m_i \dot{\mathbf{v}}_{i,k} \dot{\mathbf{q}}_k \quad (45)$$

$$\mathbf{M}_{i,inr} = \mathbf{M}_{i,inr:m} \ddot{\mathbf{q}}_k + \mathbf{M}_{i,inr:v}$$

$$\mathbf{F}_{i,inr} = \mathbf{F}_{i,inr:m} \ddot{\mathbf{q}}_k + \mathbf{F}_{i,inr:v}. \quad (46)$$

Using (4) and (46), \mathbf{M}_{wgt} and \mathbf{V}_{wgt} may be formulated as defined in (48), shown below, where (47), shown below, defines the force and moment vectors for the \mathbf{V}_{wgt} .

$$\mathbf{M}_{i,ex:v} = \mathbf{M}_{i,inr:v} + \mathbf{M}_{i,el} + \mathbf{M}_{i,act},$$

$$\mathbf{F}_{i,ex:v} = \mathbf{F}_{i,inr:v} + \mathbf{F}_{i,gr} + \mathbf{F}_{i,act} \quad (47)$$

$$\mathbf{M}_{wgt} = \sum_i (\boldsymbol{\omega}_{i,k} \cdot \mathbf{M}_{i,inr:m} + \mathbf{v}_{i,k} \cdot \mathbf{F}_{i,inr:m})$$

$$\mathbf{V}_{wgt} = \sum_i (\boldsymbol{\omega}_{i,k} \cdot \mathbf{M}_{i,ex:v} + \mathbf{v}_{i,k} \cdot \mathbf{F}_{i,ex:v}). \quad (48)$$

MATLAB requires the ODEs be formulated as a set of first-order equations. As a result, (42) is reformulated into (49), shown below, where $\dot{\mathbf{X}} = [\dot{\mathbf{q}}^T, \ddot{\mathbf{q}}^T]^T$ and \mathbf{I} is the identity matrix

$$\begin{bmatrix} \mathbf{I} & \mathbf{0} \\ \mathbf{0} & \mathbf{M}_{wgt} \end{bmatrix} \dot{\mathbf{X}} = \begin{bmatrix} \dot{\mathbf{q}} \\ \mathbf{V}_{wgt} \end{bmatrix}. \quad (49)$$

Two different initial conditions are used for the numerical solutions generated in the remainder of this section. For the zero actuation case study with all input tensions equaling zero, the initial β_i is -0.001 m⁻¹ and the initial γ_i and ε_i are zero to avoid the singularity when $\beta_i = \gamma_i = k_i = 0$. For the actuated response, the initial condition becomes the continuum robot's zero actuation static equilibrium (calculated using the solution of the virtual power statics model for zero actuation, discussed below). For all case studies in this paper, an eight-disk cable-driven continuum robot is simulated with material and geometric properties detailed in Table I.

Using this numerical model, simulations were performed to compare the dynamic response with alternative methods of calculating the mechanics, as discussed in Section VI. Three

case-studies were considered: 1) the zero actuation response; 2) the planar actuation response; and 3) out-of-plane actuation response.

In addition, as discussed previously and in Section II, the virtual power may also be used to generate a model for the static equilibrium of the continuum robot. This is found by neglecting the inertial effects in the model, resulting in a formulation of the external forces $\mathbf{F}_{i,ex:st}$ and moments $\mathbf{M}_{i,ex:st}$ for the static model, as in (50), shown below. However, a slight modification to the model is required to transform the dynamic model into a static model. The friction force is dependent on the velocity of the cable sliding through the cable routing holes. In this static model, the saturation function $sat(\dot{d}_{i,j,disk})$ will be replaced by either -1 or $+1$. The sign will depend on the "starting" point for the loading or unloading—for example, if loading from zero actuation, the function is -1 , because the friction will resist the transmission of force from the base to the tip. However, when "unloaded" from a higher tension to a lower tension, the friction will resist the reduction in tension from the base to the tip, requiring use of $+1$. As discussed previously, this model does not account for higher static friction allowed when considering a stick-slip friction model

$$\mathbf{M}_{i,ex:st} = \mathbf{M}_{i,el} + \mathbf{M}_{i,act}$$

$$\mathbf{F}_{i,ex:st} = \mathbf{F}_{i,gr} + \mathbf{F}_{i,act}. \quad (50)$$

These external forces and moments are then used to calculate the virtual power variation ΔP_{st} , as in (51), shown below. Because there are no derivatives in the equation, it is a set of coupled algebraic equations, where the number of variables equals the number of equations. MATLAB's "fsolve" function [32] is used to find the set of generalized coordinate for which this variation is within the numerical error tolerance of zero.

$$\Delta P_{st} = \sum_i (\boldsymbol{\omega}_{i,k} \cdot \mathbf{M}_{i,ex:st} + \mathbf{v}_{i,k} \cdot \mathbf{F}_{i,ex:st}) = 0. \quad (51)$$

As discussed in Section IV-D, the friction model uses an iterative solver to implement the simultaneous calculation of cable-disk contact forces and the tension along the length of the continuum robot. In order to determine the number of iterations for the cable tension/friction force convergence, the virtual power static equilibrium script is used to track the change in subsegment cable tension at each iteration. Fig. 5 shows the convergence of the contact forces for an eight disk robot with a prescribed tension of 10 N in cable 1 (see Fig. 1) at static equilibrium. This 10 N tension is the maximum tension applied in the subsequent analyses, and the maximum number of iterations will be needed for the maximum actuating tension.

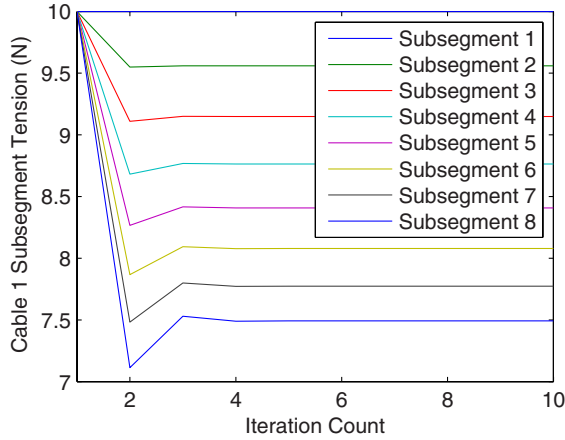


Fig. 5. Convergence of contact force magnitudes for an eight-disk continuum robot over ten iterations.

TABLE II
MAXIMUM CABLE TENSION ERROR FOR EACH ITERATION

Iter.	Error (%)	Iter.	Error (%)	Iter.	Error (%)
1	33.47	4	$3.788 \cdot 10^{-2}$	7	$5.867 \cdot 10^{-6}$
2	5.059	5	$2.338 \cdot 10^{-3}$	8	$2.524 \cdot 10^{-7}$
3	$5.028 \cdot 10^{-1}$	6	$1.241 \cdot 10^{-4}$	9	$1.049 \cdot 10^{-8}$

Table II shows the maximum percent error at each iteration for the cable subsegments (in each case, the maximum error was in subsegment 8). Three iterations were chosen—the maximum subsegment tension error will be less than 1% in the highest actuation case.

B. Zero Actuation Simulation

Fig. 6 illustrates the dynamic response of the β curvatures of the continuum robot's second, fourth, sixth, and eighth subsegments with zero tension in the three cables. This subset of the eight curvature responses presents the curvatures change along the continuum robot without the need to extraneously plot each subsegment's response. The model's initial condition is -0.001 for each β curvature and zero for the γ curvatures and the ε twist angles. This is equivalent to supporting the robot in this initial condition then removing this support at time $t = 0$. The continuum robot's zero actuation simulation results in sustained oscillations of the continuum robot's curvatures around a stable point. Because the cable tensions are all zero, there is no contact force between the cabling and the disks, resulting in zero friction along the arm. Because the friction is the only dissipative force in the model, the energy of the continuum robot in the zero actuation simulation is constant.

Fig. 7 shows the first oscillation of the continuum robot after release: the robot initially drops over 0.1342 s, then springs up over 0.1036 s.

C. In-Plane Actuation Simulation

Fig. 8 illustrates the dynamic responses of the selected β curvatures of the virtual power dynamic model in response to a step input of a 5 N tension in cable 1 (see Fig. 1) from the initial condition of zero actuation static equilibrium. Because the ac-

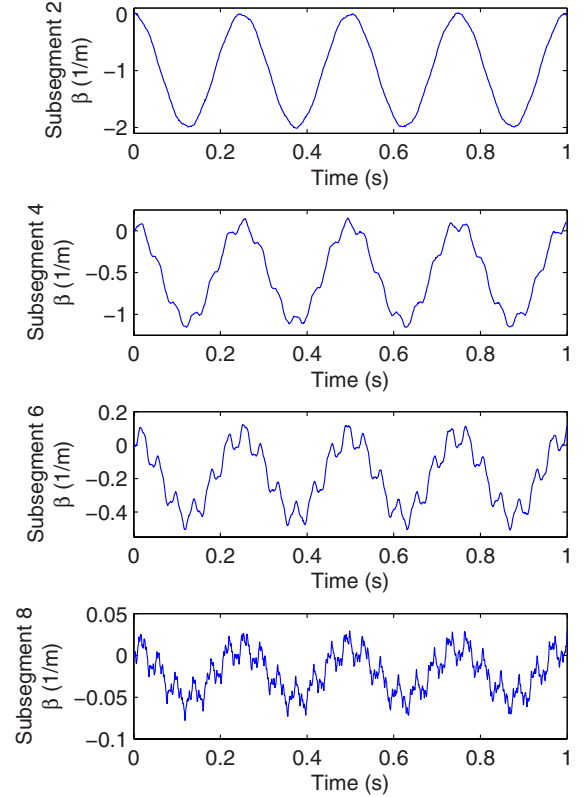


Fig. 6. Zero actuation response β curvatures for subsegments 2, 4, 6, and 8.

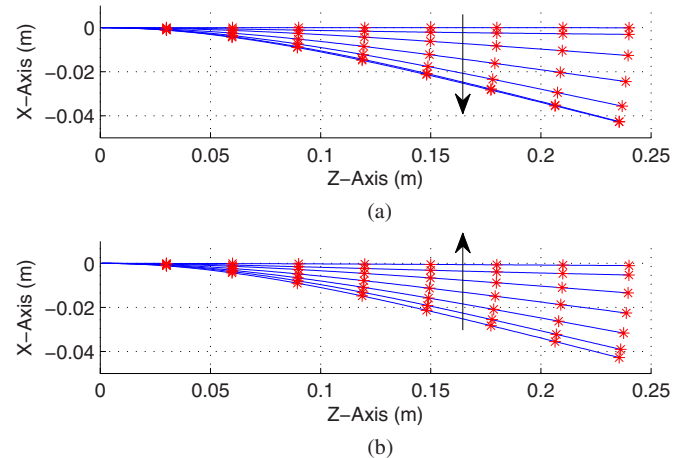


Fig. 7. Time-lapse of zero actuation response. (a) Initial drop over 0.1342 s, (b) Initial return over 0.1036 s. Each frame's seven illustrations are equally spaced over the interval.

tuation remains in the x - z plane due to the purely x -component of the hole radius $r_{icl,1}$ defined in (28), the dynamic response will remain in the x - z plane and the γ curvature and the ε twist angle will remain zero. Unlike Fig. 6, the nonzero actuation will cause a contact force between the cabling and disk, leading to friction that dampens the oscillations. In addition, because of the use of step functions to actuate the virtual systems, preliminary simulations demonstrated the need to add numerical dampening terms to the simulation to reduce the speed of oscillations and improve their stability. As a result, rate-dependent dampening for the bending and torsional vibrations

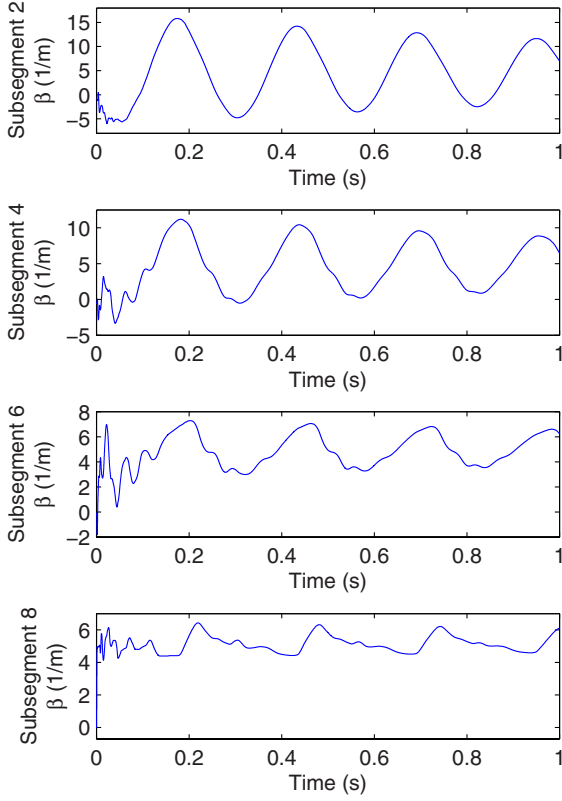


Fig. 8. Cable 1 actuation β curvatures for subsegments 2, 4, 6, and 8.

are defined in (52) and (53), shown below, where $M_{i,bD}$ is the bending dampening moment, $M_{i:(i-1),tD}$ and $M_{i:i,tD}$ are the torsional dampening moments, and C_b and C_t are the bending and torsional mode dampening parameters. The subsegment's dampening moments may be formulated into a resultant moment for each disk's $M_{i,Dmp}$ using (54), shown below. This term is added to the other moment terms in (47). Suitable values for these terms were found to be $C_b = 10^{-6} \text{N}\cdot\text{m}^2\cdot\text{s}$ and $C_t = 10^{-5} \text{N}\cdot\text{m}\cdot\text{s}$ based on preliminary simulations

$$M_{i,bD} = C_b \dot{k}_i \mathbf{R}_{i-1} [-s_{\varphi_i}, c_{\varphi_i}, 0]^T \quad (52)$$

$$M_{i:(i-1),tD} = C_t \dot{\varepsilon}_i \hat{z}_{i-1}, \quad M_{i:i,tD} = -C_t \dot{\varepsilon}_i \hat{z}_i \quad (53)$$

$$M_{i,dmp} = \begin{cases} M_{i:i,tD} + M_{(i+1):i,tD} \\ + M_{i+1,bD} - M_{i,bD}, & i < N \\ M_{i:i,tD} - M_{i,bD}, & i = N. \end{cases} \quad (54)$$

Fig. 9 shows the two motions of the continuum robot after application of the tension. The robot initially deflects downward over 0.02682 s, then snaps upward over 0.14292 s. As in Fig. 7, each panel shows seven illustrated configurations equally spanning these two time spans.

D. Out-of-Plane Actuation Simulation

Fig. 10 illustrates the dynamic responses of the β and γ curvatures of a dynamic model in response to a step input of a 5 N tension in cable 2 (see Fig. 1) from the initial condition of zero actuation static equilibrium.

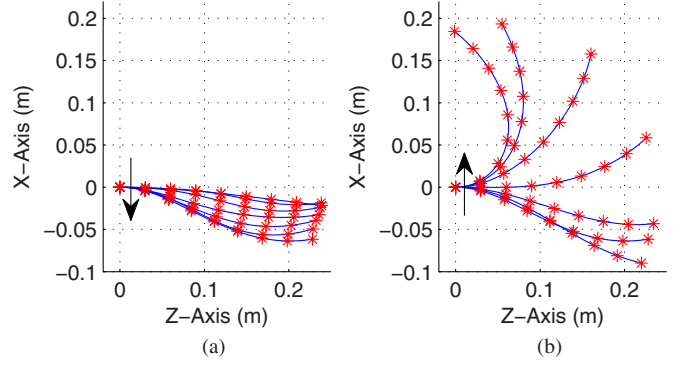


Fig. 9. Time-lapse of cable 1 actuation response. (a) Initial downward motion over 0.0659 s. (b) Initial upward motion over 0.0988 s. Each frame's seven illustrations are equally spaced over the time intervals.

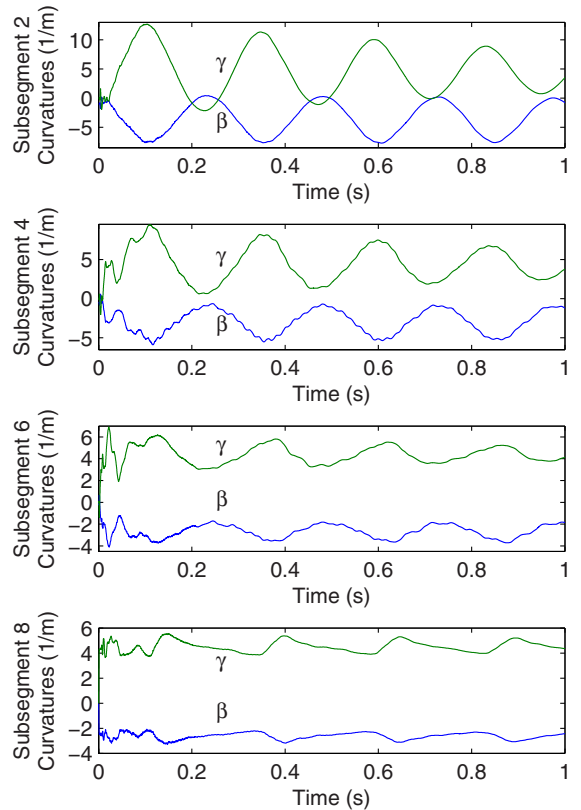


Fig. 10. Cable 2 actuation curvatures for subsegments 2, 4, 6, and 8.

Fig. 11 illustrates the dynamic response of the torsional twist angle ε . Unlike the first two case studies, because of the out-of-plane actuation, the gravitational loading will cause twist along the length of the subsegments. For the scaling of the current continuum robot, the magnitude and impact of these torsional vibrations is relatively small compared with the impact of variation in curvatures. However, as macro-scale robots are considered and the distributed mass along the continuum arm increases, this effect will significantly impact the continuum robot shape. The numerical dampening discussed in Section V-C causes the dampening of the high-frequency oscillations. As a result, as the simulation continues, the oscillations of subsegments 2 and 4 increase

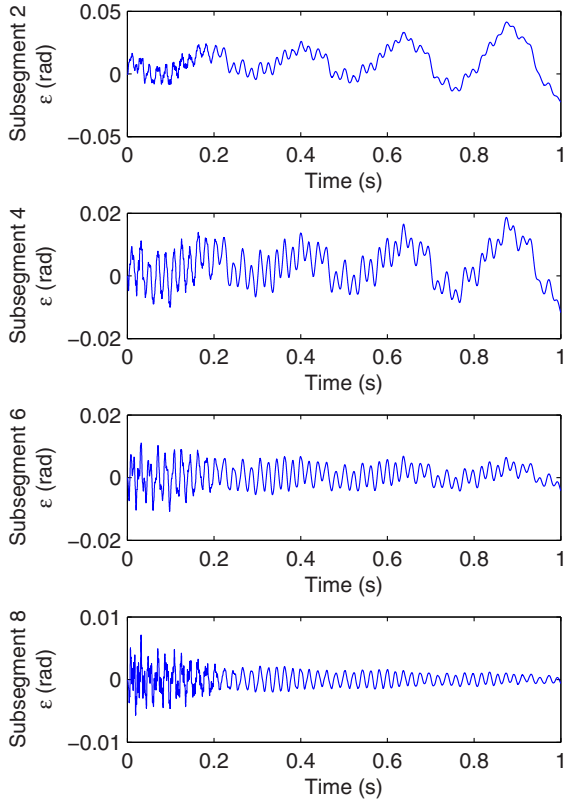


Fig. 11. Cable 2 twist angle trajectories for subsegment 2, 4, 6, and 8.

in magnitude. This is due to the coupling between the twist angle and the curvatures. As the curvatures oscillate (shown in Fig. 10), the geometry of the continuum arm changes, particularly the distance between the disks and the x - z plane. This causes changes in the twist angle. The dampening and friction will converge the mutual oscillations to equilibrium over time.

VI. CROSS-VALIDATION: NUMERICAL AND EXPERIMENTAL

In this section, the continuum robot dynamic responses are compared with experimental results and other numerical models. For each case study, the steady-state component of the dynamic responses will be compared with the virtual power static equilibrium (discussed in Section V-A). In Section VI-A, the steady-state and transient components of the zero actuation dynamic response will also be compared with a dynamic finite-element analysis (FEA) of the continuum robot. In Section VI-B, the steady-state component of the in-plane actuation dynamic response will also be compared with the measured experimental static equilibrium of a continuum robot prototype. In Section VI-C, no additional methods of comparison will be provided, but the simulations will each compare the two sets of curvatures and twist angle.

A. Zero Actuation Validation

Two key properties of the zero actuation dynamic response shown in Fig. 6 have been analyzed and compared with alternative methods of numerical modeling. First, the steady-state

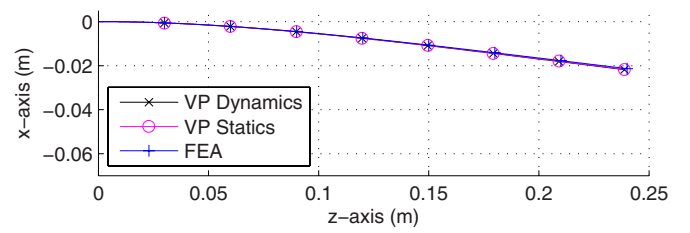


Fig. 12. Comparison of the zero actuation steady-state component of the dynamic response, the static virtual power equilibrium, and the FEA static equilibrium.

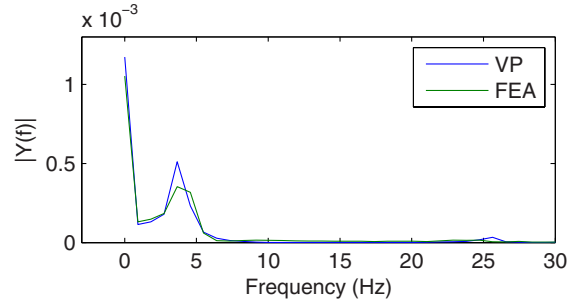


Fig. 13. Comparison of frequency response magnitude for dynamic virtual power and dynamic finite-element analysis models for disk 1.

component of the dynamic response will be compared with the static equilibria generated using two alternative numerical methods. Second, frequency domain analysis will compare the transient component of the dynamic response simulated using the virtual power method with the transient response of a dynamic finite-element simulation of the continuum robot.

Fig. 12 compares three simulations for the zero actuation case of the continuum robot: 1) the steady-state component of the dynamic response in Section V-B; 2) the equilibrium of the static virtual power model (discussed in Section V-A); and 3) the equilibrium of a static finite-element model found using COMSOL's Structural Mechanics module's 3-D linear elasticity model with a "Fine" mesh [33]. Each case uses the numerical properties provided in Table I. As seen in Fig. 12, the three plots are nearly superimposed on one another. Calculating the error of the virtual power simulation disk positions relative to the finite-element simulation (because the FEA simulation is the highest fidelity), the maximum disk position error for the dynamic steady-state response is 0.5188%, and for the virtual power static equilibrium: 0.4848%.

In addition to the steady-state component of the dynamic response, the transient component of the dynamic response is also analyzed. In order to quantify this transient response, a fast Fourier transform (FFT), [32], was performed on the vertical oscillations computed using: 1) the virtual power dynamics model, and 2) the dynamic FEA model. For the virtual power dynamics model, the curvature responses (illustrated in Fig. 6) are mapped into time-varying disk displacements. The oscillations of the x -displacement of the disks' centers of mass for this response are then compared with the simulated response generated using the dynamic FEA. Fig. 13 illustrates the frequency response for the first disk in the continuum robot for the two cases. There is a strong correlation between the frequency responses, with a

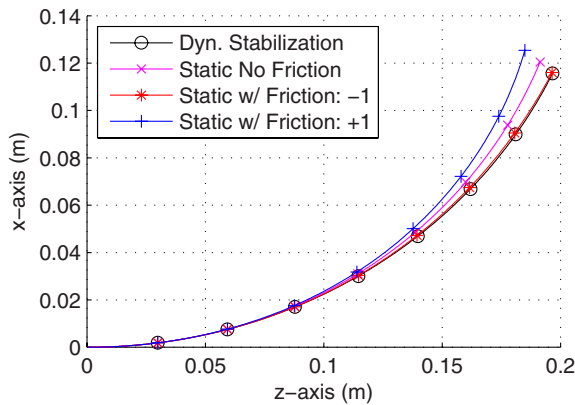


Fig. 14. Comparison of the stabilization of virtual power dynamic model with friction to static equilibrium models with and without friction for $T_1 = 5$ N.

similar zero-frequency magnitude (corresponding to the steady-state response) and a significant peak at the 3.6621 and 4.5776 Hz frequencies. Disk 1's frequency response is representative of the other disks responses.

The discrepancy between the two frequency profiles is due to several factors. First, because the virtual power dynamics solver uses a variable time step to solve the dynamics, the simulation results were resampled at a high frequency (30 kHz) to create a uniform step-size between data points. This resampling used linear interpolation for times at which there was not a matching data point. Second, COMSOL was limited in the number of discrete points the simulation could save during the simulation. For the 1 s simulation used to characterize the dynamics sampling at a rate of 5 kHz, the results file exceeded 1 GB, due to the mesh density. These 5 kHz results were then resampled like the virtual power dynamic response to 30 kHz to ensure equal fundamental frequencies. Third, the spatial discretizations between the two models differs on the orders of magnitude and will slightly influence the resulting dynamic responses.

B. In-Plane Actuation Validation

Unlike the zero actuation validation, the friction model will cause the dampening of the dynamic response toward the steady-state solution, preventing the application of conventional frequency domain analysis methods for the transient response. However, because of the formulation of the friction model for this dynamic model in Section IV-D, the friction actually approaches zero as the continuum robot velocity approaches zero. Without the numerical dampening introduced in Section V-C, the simulation's steady-state response approaches the zero-friction static equilibrium configuration; however, the introduction of the dampening effects causes the response to dampen to the lower bound of the virtual power static equilibrium model with friction, as shown in Fig. 14. This figure illustrates the steady-state component of the dynamic response, as well as three cases for the static equilibrium: 1) the case with zero friction; 2) the case with the friction saturation function (38) equal to +1; and 3) the case with the friction saturation function equal to -1.

In addition, these virtual power models have also been compared with experimental results. Fig. 15 shows the experimental

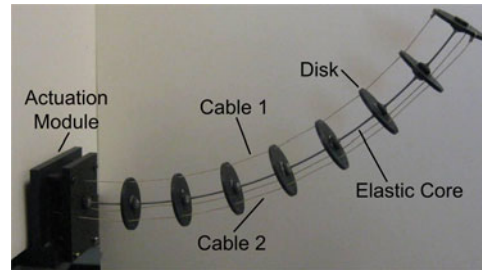


Fig. 15. Prototype used for experimental validation. Cables are tensioned using hanging weights routed over pulleys in the actuation module.

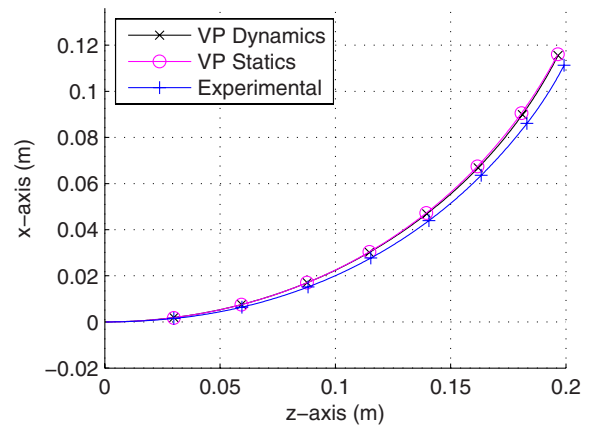


Fig. 16. Comparison of in-plane actuation dynamic virtual power response steady-state component to the measured static equilibrium of a continuum robot prototype and the calculated static virtual power model equilibrium.

test platform used to validate the dynamic modeling approach. A spring steel core (ASTM A228, 1.04 mm diameter, 240 mm long) was used with four disks (ABS plastic, 31 mm diameter, 2 mm thick, 30 mm disk spacing) mounted along the core using cyanoacrylate (Loctite 401, Uline, Pleasant Prairie, WI, USA). Hanging weights were used to tension the cables, with PTFE-coated fiberglass thread (0.43 mm diameter) used as the cabling. Three transmission cables were routed through the disks at three equally spaced holes offset 12.5 mm from center. These properties match the properties used to simulate the model presented in Table I. The shape was measured by photographing the disks along the continuum robot in profile, then calculating their angles by postprocessing the images. The bending plane angle θ_i was found for each subsegment by subtracting the two surrounding disks' angles, and the subsegments curvatures were found by dividing θ_i by L_0 . The error of this image processing step was estimated by determining the angles of gradations on a protractor, then determining the associated curvature for a given difference in angle. This was compared with the predicted curvature for the known difference in angle. The maximum curvature error was found to be 1.637%.

Fig. 16 compares the steady-state component of the dynamic virtual power response with the experimental results and static virtual power equilibrium for a 5 N tension applied in cable 1. The maximum error between the disk positions of experimental results and the dynamic virtual power response steady-state component is 2.1961% in disk 8, and between the disk positions

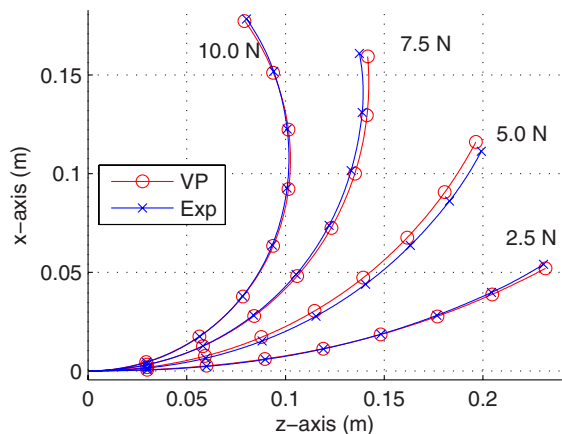


Fig. 17. Equilibrium configurations of static virtual power continuum robot model with friction compared with experimentally measured static equilibria at cable 1 tensions of 2.5, 5.0, 7.5, and 10.0 N.

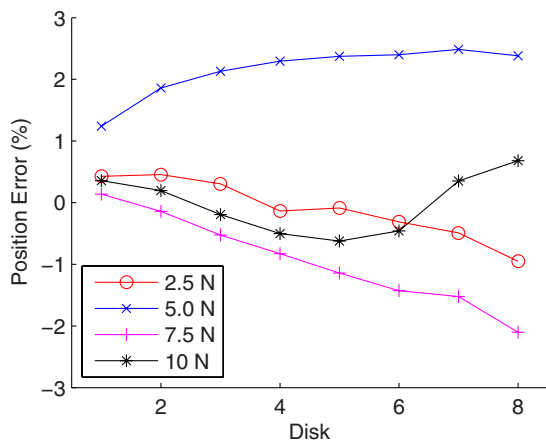


Fig. 18. Error of disk positions relative to the experimentally measured disk positions for actuation tensions of 2.5, 5, 7.5, and 10 N in cable 1.

of the experimental results and the static virtual power model equilibrium is 2.4866% in disk 7.

Beyond the single actuation case presented in Fig. 16, Fig. 17 compares experimental results for a range of actuation tensions ranging from 2.5 to 10 N with the associated calculated static equilibria using the virtual power model. Fig. 18 quantifies the percent error of the disk positions of the virtual power static equilibrium relative to the experimental results (a positive error correlates to “overshooting” the experimental configuration, like the 5 N case). Because the error in this type of serial manipulator propagates from the base, the most significant error is the disk 1 errors. A maximum disk 1 position error of 1.2405% was seen in the 5.0 N actuation case. This error is less than the measurement error discussed previously, leading to the conclusion that the errors between the measured and simulated static equilibria are within the measurement range of error.

C. Out-of-Plane Actuation Validation

The out-of-plane dynamic response described in Section V-D tensions cable 2 in the continuum robot, leading to a deformation out of the x - z plane. Unlike the previous section in which

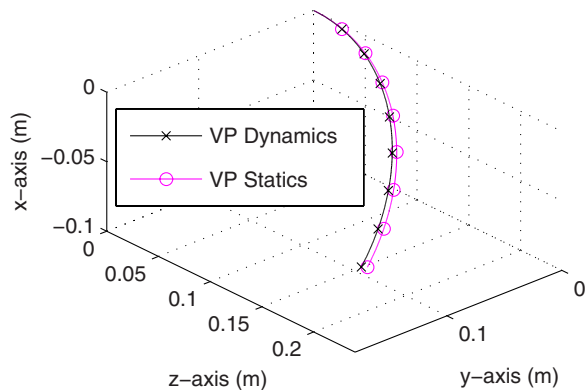


Fig. 19. Steady-state component of dynamic virtual power model response compared with static virtual power simulation of continuum robot equilibrium with a cable 2 tension of 5 N.

the continuum robot was confined to a single plane of motion, the torsional twist along the robot creates a generalized spatial shape for the continuum robot. It is not simply the in-plane response rotated by 120° . As a result, the measurement used in the previous section (estimating subsegment curvatures using the disk angle extrapolated from photographs) is not applicable to this case. However, due to the scaling of this manipulator, the torsional effects are not as significant as they would be in a longer and/or more massive structure, as discussed in Section V-D. The stabilization of the dynamic response is still compared with the static virtual power, as shown in Fig. 19. Due to the interaction between the curvatures and torsional twist angle, there is a greater error between the dynamic model’s steady-state response and the static model’s static equilibrium compared with the in-plane actuation, but the maximum error remains only 2.0926% at disk 5 for the dynamic steady-state response compared with the static equilibrium.

VII. CONCLUSION

This paper presented a novel dynamic model for continuum robotics using the principle of virtual power. The resulting numerical model was a series of coupled first-order ODEs, allowing for the numerical integration of the mass-matrix weighted set of differential equations. A model for the static equilibrium was also derived using the same formulation by neglecting inertial effects. The modeling approach was validated by comparing the simulated zero actuation, in-plane actuation, and out-of plane actuation dynamics responses to static simulations using the virtual power model, dynamic FEA, and experimental results.

Future work will include broader application of the methodology to continuum robotics and investigations into inverse mechanics. Broader application of the modeling methodology will include consideration of alternate actuation modes (e.g., rods or pneumatic muscles), elastic cores (e.g., pneumatic bellows), dynamic friction models (e.g., Dahl friction [34]), robots with multiple independently actuated segments to generate different mode shapes along the robot and time-varying control input trajectories. Future investigations into inverse mechanics will explore ways in which control commands may be optimally generated (based on the task-space redundancy relative to the control

parameters) to meet a user's desired dynamic performance of a robot in tasks such as endpoint positioning, object grasping, or generating forces/moments at the base of the continuum robot.

REFERENCES

- [1] J. Qing-xuan, C. Ming, and S. Han-xu, "Research on the numerical method of nonlinear rigidity/flexibility coupling dynamics equations of flexible-joint flexible-link space manipulator," in *Proc. 2nd Int. Conf. Intell. Comput. Technol. Autom.*, 2009, pp. 915–919.
- [2] J. H. Davis and R. M. Hirschhorn, "A model for the embedded tendon control of a slender three-dimensional flexible robot link," *Dyn. Control*, vol. 4, pp. 185–208, 1994.
- [3] S. Hirose, *Biologically Inspired Robots: Snake-Like Locomotors and Manipulators*. Oxford, U.K.: Oxford Univ. Press, 1993.
- [4] R. J. Webster, III and B. A. Jones, "Design and kinematic modeling of constant curvature continuum robots: A review," *Int. J. Robot. Res.*, vol. 29, no. 13, pp. 1661–1683, 2010.
- [5] G. S. Chirikjian and J. W. Burdick, "A modal approach to hyper-redundant manipulator kinematics," *IEEE Trans. Robot. Autom.*, vol. 10, no. 3, pp. 343–354, Jun. 1994.
- [6] E. Tatlicioglu, I. D. Walker, and D. M. Dawson, "Dynamic modelling for planar extensible continuum robot manipulators," in *Proc. IEEE Conf. Robot. Autom.*, Rome, Italy, 2007, pp. 1357–1362.
- [7] I. S. Godage, D. T. Branson, E. Guglielmino, G. A. Medrano-Cerda, and D. G. Caldwell, "Dynamics for biomimetic continuum arms: A modal approach," in *Proc. IEEE Int. Conf. Robot. Biomimet.*, 2011, pp. 104–109.
- [8] B. A. Jones, R. L. Gray, and K. Turlapati, "Three dimensional statics for continuum robotics," in *Proc. IEEE/RSJ Int. Conf. Intell. Robot. Syst.*, St. Louis, MO, USA, 2009, pp. 2659–2664.
- [9] F. Renda, M. Cianchetti, M. Giorelli, A. Arienti, and C. Laschi, "A 3-D steady-state model of a tendon-driven continuum soft manipulator inspired by the octopus arm," *Bioinspir. Biomim.*, vol. 7, art. ID 025006, 2012.
- [10] D. C. Rucker, R. J. Webster, III, G. S. Chirikjian, and N. J. Cowan, "Equilibrium conformations of concentric-tube continuum robots," *Int. J. Robot. Res.*, vol. 29, no. 10, pp. 1263–1280, Sep. 2010.
- [11] D. C. Rucker and R. J. Webster, III, "Statics and dynamics of continuum robots with general tendon routing and external loading," *IEEE Trans. Robot.*, vol. 27, no. 6, pp. 1033–1044, Dec. 2011.
- [12] J. Spillmann and M. Teschner, "CORDE: Cosserat rod elements for the dynamic simulation of one dimensional elastic objects," in *Proc. Eurographics/ACM SIGGRAPH Symp. Comput. Animat.*, 2007, pp. 63–72.
- [13] H. Lang, J. Linn, and M. Arnold, "Multi-body dynamics simulation of geometrically exact Cosserat rods," *Multibody Syst. Dyn.*, vol. 25, no. 3, pp. 285–312, Nov. 2010.
- [14] G. S. Chirikjian, "Hyper-redundant manipulator dynamics: A continuum approximation," *Adv. Robot.*, vol. 9, no. 3, pp. 217–243, 1995.
- [15] I. A. Gravagne, C. D. Rahn, and I. D. Walker, "Large deflection dynamics and control for planar continuum robots," *IEEE/ASME Trans. Mechatronics*, vol. 8, no. 2, pp. 299–307, Jun. 2003.
- [16] W. McMahan, B. A. Jones, and I. D. Walker, "Design and implementation of a multi-section continuum robot: Air-Octor," in *Proc. IEEE/RSJ Int. Conf. Intell. Robot. Syst.*, 2005, AB, Canada, pp. 2578–2585.
- [17] D. B. Camarillo, C. F. Milne, C. R. Carlson, M. R. Zinn, and J. K. Salisbury, "Mechanics modeling of tendon-driven continuum manipulators," *IEEE Trans. Robot.*, vol. 24, no. 6, pp. 1262–1273, Dec. 2008.
- [18] K. Xu and N. Simaan, "An investigation of the intrinsic force sensing capabilities of continuum robots," *IEEE Trans. Robot.*, vol. 24, no. 3, pp. 576–587, Jun. 2008.
- [19] N. Simaan, R. Taylor, and P. Flint, "A dexterous system for laryngeal surgery," in *Proc. IEEE Int. Conf. Robot. Autom.*, New Orleans, LA, USA, 2004, pp. 351–357.
- [20] W. McMahan, V. Chitrakaran, M. Csencsits, D. Dawson, I. D. Walker, B. A. Jones, M. Pritts, D. Dienno, M. Grissom, and C. D. Rahn, "Field trials and testing of the OctArm continuum manipulator," in *Proc. IEEE Int. Conf. Robot. Autom.*, Orlando, FL, USA, 2006, pp. 2336–2341.
- [21] *Bionic Handling Assistant*, Festo, Esslingen, Germany, 2010.
- [22] Y. Shapiro, A. Wolf, and K. Gabor, "Bi-bellows: Pneumatic bending actuator," *Sens. Actuators A, Phys.*, vol. 167, no. 2, pp. 484–494, Jun. 2011.
- [23] M. De Volder and D. Reynaerts, "Pneumatic and hydraulic microactuators: A review," *J. Micromech. Microeng.*, vol. 20, art. ID 043001, Apr. 2010.
- [24] J. Lock, G. Laing, M. Mahvash, and P. E. Dupont, "Quasistatic modeling of concentric tube robots with external loads," in *Proc. IEEE/RSJ Int. Conf. Intell. Robot. Syst.*, 2010, pp. 2325–2332.
- [25] D. C. Rucker, B. A. Jones, and R. J. Webster, III, "A geometrically exact model for externally loaded concentric-tube continuum robots," *IEEE Trans. Robot.*, vol. 26, no. 5, pp. 769–780, Jan. 2010.
- [26] K. Xu and N. Simaan, "Analytic formulation for kinematics, statics, and shape restoration of multibackbone continuum robots via elliptic integrals," *ASME J. Mech. Robot.*, vol. 2, pp. 011006–1–13, Feb. 2010.
- [27] W. S. Rone and P. Ben-Tzvi, "Continuum manipulator statics based on the principle of virtual work," presented at the ASME Int. Mech. Eng. Cong. Expo., Houston, TX, USA, 2012.
- [28] T. R. Kane and D. A. Levinson, "The use of Kane's dynamical equations in robotics," *Int. J. Robot. Res.*, vol. 2, no. 3, pp. 3–21, 1983.
- [29] M. Haghshenas-Jaryani and G. Vossoughi, "Modeling and sliding mode control of a snake-like robot with holonomic constraints," in *Proc. IEEE Int. Conf. Robot. Biomimet.*, 2009, pp. 454–461.
- [30] W. Zhuang, X. Liu, C. Fang, and H. Sun, "Dynamic modeling of a spherical robot with arms by using Kane's method," in *Proc. Int. Conf. Nat. Comput.*, 2008, pp. 373–377.
- [31] L. J. Everett, "An extension of Kane's method for deriving equations of motion of flexible manipulators," in *Proc. IEEE Int. Conf. Robot. Autom.*, 1989, pp. 716–721.
- [32] (2013, Mar. 23). [Online]. Available: MathWorks. Internet: <http://www.mathworks.com/>
- [33] COMSOL. (2013, Mar. 23). Structural mechanics module. [Online]. Available: Internet: <http://www.comsol.com/products/structural-mechanics/>
- [34] J. Jung, R. S. Penning, N. J. Ferrier, and M. R. Zinn, "A modeling approach for continuum robotic manipulators: effects of nonlinear internal device friction," in *Proc. IEEE/RSJ Int. Conf. Intell. Robot. Syst.*, 2011, pp. 5139–5146.



William S. Rone (S'11) received the B.S. degree (*summa cum laude*) in mechanical engineering from The George Washington University (GWU), Washington, DC, USA, in 2010. He is currently working toward the Ph.D. degree in mechanical engineering with the Robotics and Mechatronics Laboratory, GWU.

His research interests include modeling, sensing, task planning, and control of continuum robots for applications in dynamic active stabilization and maneuvering of mobile robots using a continuum tail.

Mr. Rone received the SMART Scholarship from the U.S. Department of Defense and is sponsored by the Air Force Research Laboratory Aerospace Systems Directorate and the Robotics and Mechatronics Laboratory. He is a member of the American Society of Mechanical Engineers.



Pinhas Ben-Tzvi (S'02–M'08–SM'12) received the B.S. degree (*summa cum laude*) in mechanical engineering from the Technion—Israel Institute of Technology, Haifa, Israel, in 2000 and the M.S. and Ph.D. degrees in mechanical engineering from the University of Toronto, Toronto, ON, Canada, in 2004 and 2008, respectively.

He is currently an Assistant Professor with the Department of Mechanical and Aerospace Engineering and the Founding Director of the Robotics and Mechatronics Laboratory at The George Washington University, Washington, DC, USA. Before joining the University of Toronto in 2002, he was an R&D Engineer with General Electric Medical Systems Company, developing medical diagnostic robotic and mechatronic systems. His current research interests include robotics and autonomous systems, mechatronics, dynamic systems and control, mechanism/machine design and integration, and sensing and actuation. Applications include robust dynamic stabilization and agile maneuvering of mobile robots using intelligent biomimetic robotic tails; autonomous mobile robot mobility and manipulation and modular and reconfigurable mobile robotics for search and rescue, environment monitoring, and defense; advanced devices and robotic systems for medicine; haptics devices and exoskeletons for robot control and rehabilitation; and novel sensors and actuators for biomedical applications. He has authored and co-authored more than 60 peer-reviewed journal articles and refereed papers in conference proceedings and is the inventor of five U.S. patents and a Canadian patent.

Dr. Ben-Tzvi was awarded in 2013 The George Washington University School of Engineering and Applied Science Outstanding Young Researcher Award and Outstanding Young Teacher Award, as well as several other honors and awards. He is a member of the American Society of Mechanical Engineers.